

A 19.9%-efficient ultrathin solar cell based on a 205-nm-thick GaAs absorber and a silver nanostructured back mirror

Hung-Ling Chen¹, Andrea Cattoni¹ , Romaric De Lépinau^{1,2}, Alexandre W. Walker^{1,3,5} , Oliver Höhn³, David Lackner³, Gerald Siefer³, Marco Faustini⁴, Nicolas Vandamme¹, Julie Goffard^{1,2}, Benoît Behaghel¹, Christophe Dupuis¹, Nathalie Bardou¹, Frank Dimroth^{1,3}  and Stéphane Collin^{1,2*} 

Conventional photovoltaic devices are currently made from relatively thick semiconductor layers, ~150 μm for silicon and 2–4 μm for Cu(In,Ga)(S,Se)₂, CdTe or III–V direct bandgap semiconductors. Ultrathin solar cells using 10 times thinner absorbers could lead to considerable savings in material and processing time. Theoretical models suggest that light trapping can compensate for the reduced single-pass absorption, but optical and electrical losses have greatly limited the performances of previous attempts. Here, we propose a strategy based on multi-resonant absorption in planar active layers, and we report a 205-nm-thick GaAs solar cell with a certified efficiency of 19.9%. It uses a nanostructured silver back mirror fabricated by soft nanoimprint lithography. Broadband light trapping is achieved with multiple overlapping resonances induced by the grating and identified as Fabry–Perot and guided-mode resonances. A comprehensive optical and electrical analysis of the complete solar cell architecture provides a pathway for further improvements and shows that 25% efficiency is a realistic short-term target.

The efficiency of single-junction solar cells has improved consistently over time for both crystalline silicon (c-Si) and thin-film (Cu(In,Ga)(S,Se)₂ (CIGS), CdTe, GaAs) technologies, and contributed to the cost decrease and widespread development of photovoltaic devices. Solar cells made of c-Si have reached 26.7% photoconversion efficiency using 165-μm-thick Si wafers¹. With its high optical absorption and radiative efficiency, GaAs operates close to the Shockley–Queisser limit² and has achieved a record efficiency of 29.1% with 1- to 2-μm-thick single-junction solar cells^{3,4}. On the other hand, theoretical light-trapping models suggest that the solar cell thickness can be reduced by more than one order of magnitude while preserving state-of-the-art short-circuit currents^{5,6}. Such a thickness reduction will improve industrial throughput and save scarce materials (for example, tellurium in CdTe, indium in CIGS and III–V materials) as well as help in improving the performance of solar cells. For a given density of defects, non-radiative bulk recombination decreases with thickness, allowing for the use of materials with a reduced diffusion length. For space applications, ultrathin GaAs cells show increased tolerance to high-energy particle bombardment⁷. Overall, thinning the absorber has a beneficial effect on both charge carrier collection and open-circuit voltage. The best solar cell would be an ultrathin solar cell if maximal absorption could be maintained through efficient light trapping.

Different light trapping strategies have been proposed and successfully used to compensate for the short-circuit current drop due to incomplete absorption in ultrathin layers^{8–10}. Disordered nanotextures are a conventional approach and have allowed 8.6% efficiency with only 830-nm-thick silicon layers¹¹. Front surface nanotexturing with inverted pyramid arrays coupled with a highly reflective

back mirror has been optimized for ultrathin silicon solar cells^{12–14} and led to 15.4% efficiency with 10-μm-thick c-Si layers¹². However, efficiencies exceeding 20% have only been achieved with c-Si solar cells thicker than 40 μm (ref. ¹⁵). Nanostructured back mirrors were used to increase the long-wavelength absorption in III–V/Si tandem solar cells¹⁶, and a numerical study has shown broadband absorption capabilities in 150-nm-thick CIGS solar cells¹⁷. Dielectric nanoparticles have also been successfully introduced at the rear side of CIGS solar cells with no significant impact on fill factor (FF) and open-circuit voltage (V_{oc}), leading to 12.3% efficiency with a thickness of 460 nm (ref. ¹⁸). On the contrary, a-Si:H deposited on a textured substrate shows improved absorption^{19,20} but low electrical performance. Overall, the best light trapping designs tend to avoid texturing of the absorber.

Ultrathin GaAs solar cells can be considered as a model system to investigate the potential of light trapping for high-efficiency ultrathin solar cells. Metal nanoparticles^{21,22} and nanogrids²³ can improve absorption via plasmonic resonances²⁴, but the beneficial effect is usually countered by metal absorption losses at short wavelengths. The integration of a highly reflective back mirror is a first requirement for efficient light trapping²⁵, and it can boost the V_{oc} through the photon recycling effect^{26–28}. Others have used a rough scattering Au back mirror to further enhance light trapping. They achieved 19.1% efficiency with 300-nm-thick solar cells²⁹. In contrast, front-side periodic TiO₂ nanostructures have also been combined with a flat back reflector and reached 16.2% efficiency in 200-nm-thick GaAs solar cells³⁰. State-of-the-art ultrathin GaAs solar cells are listed in Table 1. Overall, previous achievements make use of light scattering and diffraction and lie below numerical predictions for double-pass absorption.

¹Centre for Nanoscience and Nanotechnology (C2N), CNRS, University Paris-Sud/Paris-Saclay, Palaiseau, France. ²Institut Photovoltaïque d'Île-de-France (IPVF), Palaiseau, France. ³Fraunhofer Institute for Solar Energy Systems (ISE), Freiburg, Germany. ⁴Laboratoire Chimie de la Matière Condensée de Paris, Sorbonne Université, CNRS, Collège de France, Paris, France. ⁵Present address: National Research Council of Canada, Ottawa, Ontario, Canada.

*e-mail: stephane.collin@c2n.upsaclay.fr

Table 1 | Comparison of record thin and ultrathin single-junction GaAs solar cell performances with different absorber thicknesses

	Absorber thickness, t (nm)	J_{sc} (mA cm ⁻²)	J_{sc} /double-pass absorption	V_{oc} (V)	FF	Efficiency (%)
Refs. ^{3,4}	≥1,000	29.68	0.94	1.122	0.865	29.1
Ref. ²⁹	300	24.5	0.94	1.000	0.778	19.1
Ref. ³⁰	200	21.96	0.94	0.942	0.78	16.2
This work	205	24.64	1.05	1.022	0.792	19.9

J_{sc} values are normalized by the results of an ideal double-pass absorption model ($A = 1 - e^{-2\alpha t}$) to highlight the light trapping capability.

In this work, we propose a light trapping strategy based on multi-resonant absorption. We demonstrate a certified efficiency of 19.9% with a 205-nm-thick GaAs solar cell using planar active layers and a Ag nanostructured back mirror with a periodic pattern. It is fabricated using a low-cost and scalable technique based on direct embossing of TiO₂ sol-gel-derived film. The back mirror induces multiple overlapping resonances that provide efficient light trapping over a broad spectral range. The short-circuit current significantly exceeds an ideal double-pass absorption model while preserving the FF and V_{oc} . A detailed analysis of the optical and electrical properties of the device shows the path to reach 25% conversion efficiency using the same light trapping scheme.

Design and fabrication of ultrathin GaAs solar cells

Ultrathin GaAs solar cells require light trapping structures to compensate for the decreased absorber volume. The rationale of the solar cell design is as follows. The III-V active layers are kept flat to avoid electronic degradation induced by increased surfaces. A periodic pattern is used to enhance absorption through multiple guided-mode resonances. The number of resonances increases with period p , but diffraction losses at shorter wavelengths ($\lambda < p$ at normal incidence) may induce optical losses in free space. For this reason, the periodic structure is designed at the backside in the form of a nanostructured metallic mirror so that diffraction in free space can only occur after double-pass absorption. For a GaAs thickness of 200 nm, we found $p = 700$ nm to be a good trade-off to keep negligible diffraction losses and create numerous resonances over the 700–900 nm wavelength range. The nanostructured back mirror is made of Ag because it has the highest reflectivity among metals in this spectral range. It is combined with localized Ni/Ge/Au ohmic contacts (surface coverage, 1%) to collect charge carriers with minimal resistive losses²⁵. The exact geometry of the grating was optimized with numerical computations based on the rigorous coupled-wave analysis (RCWA) method^{31–34} (for details, see Methods), giving a Ag square nanostructure of width $d = 420$ nm (60% of the period) and grating height $h = 120$ nm.

The epitaxial stacks were grown by metal-organic vapour phase epitaxy (MOVPE) on an n-type GaAs substrate in the following sequence: n+ GaAs top contact, n AlInP window layer, 205 nm GaAs absorber, p AlGaAs back surface field (BSF) and p+ GaAs rear contact. Note that the final solar cell structure is reversed compared to the growth order. A detailed description of the III-V semiconductor layers is provided in Supplementary Table 1. Figure 1a shows a schematic of the solar cell fabrication sequences. Details about the cell fabrication process are reported in the Methods. Step 1 begins with the fabrication of $5 \times 5 \mu\text{m}^2$ Ti/Au localized ohmic contacts on p+ GaAs every 50 μm . The uncovered area of p+ GaAs was wet chemically etched to reduce parasitic optical absorption. In step 2, large-area nanostructures were formed using soft nanoimprint lithography. TiO₂ sol-gel was spin-coated on the sample surface and printed using a PDMS mould. Figure 1b presents a scanning electron microscopy (SEM) image of the nanoimprinted two-dimensional periodic TiO₂ grating. The Ag mirror was deposited to cover conformally both ohmic contacts and

TiO₂ nanopatterns (step 3). The mirror side of the sample was then bonded to a glass host substrate using a flexible polymer, and the GaAs substrate was removed by chemical etching (step 4). Figure 1c shows a cross-sectional SEM image of a similar sample fabricated up to this step, showing the TiO₂/Ag back mirror. Subsequently, Ni/Ge/Au front contact grids were fabricated on the n+ GaAs, and solar cells with dimensions of 1×1 , 2×2 and $3 \times 3 \text{ mm}^2$ were protected with a photolithography mask in the wet-chemical etching for the mesa. Finally, a MgF₂/Ta₂O₅ 78/48 nm double-layer anti-reflection coating (DLARC) was deposited (step 5).

Performances of ultrathin GaAs solar cells

The best cell was measured in the Fraunhofer ISE calibration laboratory under standard test conditions (AM1.5G, $1,000 \text{ W m}^{-2}$, 25 °C; Supplementary Figs. 10–18). The current-voltage (J - V) characteristics and external quantum efficiency (EQE) of this cell are shown in Fig. 2. We achieved a high efficiency of 19.9% using only a 205-nm-thick GaAs absorber, with parameters $J_{sc} = 24.64 \text{ mA cm}^{-2}$, $V_{oc} = 1.022 \text{ V}$ and FF = 79.2%. The solar cell area is 4.02 mm^2 , which includes the front contact grids (~5.5% shading of the total surface) in the calculation of the current density and conversion efficiency. The curve of $1 - R$ (where R , is specular reflectance) plotted in Fig. 2b represents the total absorption above 700 nm. Its spectral features exhibit multi-resonant absorption and match perfectly with the EQE in the long-wavelength range (700–900 nm). The integral over all photon energies of the EQE with the AM1.5G solar spectrum results in an equivalent $J_{sc} = 24.39 \text{ mA cm}^{-2}$, close to the direct measurement under 1 sun illumination.

Light trapping analysis

To illustrate our light trapping designs, three different solar cells were fabricated with the same epitaxially grown semiconductor stack: as-grown on a GaAs substrate with a single-layer ARC (70-nm-thick SiN_x) (A, Fig. 3), with a flat Ag mirror and DLARC (B) and with a nanostructured Ag mirror and DLARC (C). Their J - V characteristics are compared in Supplementary Fig. 1. Their EQE values were measured using a Fourier transform photocurrent spectroscopy (FTPS) set-up calibrated with a silicon reference cell, and a microscope objective was used to focus light onto a small spot (diameter, a few 100 μm) between the wires of the front contacts to avoid shading. The results are plotted in Fig. 3a and compared to the absorption calculations in Fig. 3b. The RCWA method was used to compute the electromagnetic fields and absorption spectra in each layer of the solar cell structures. The simulations are in good agreement with the EQE measurements (Supplementary Note 4) and show a similar trend for the different structures. The light trapping effect is clearly evidenced in the long-wavelength range ($\lambda > 600 \text{ nm}$). The flat Ag mirror results in double-pass absorption with an increase of the short-circuit current of $\Delta J_{sc} = 4.4 \text{ mA cm}^{-2}$. With the nanostructured back mirror, numerous overlapping resonances contribute to further absorption enhancement and result in an additional $\Delta J_{sc} = 4.5 \text{ mA cm}^{-2}$. Theoretical short-circuit current densities J_{th} sum to $J_{th} = 25.6 \text{ mA cm}^{-2}$ for structure C. The measured

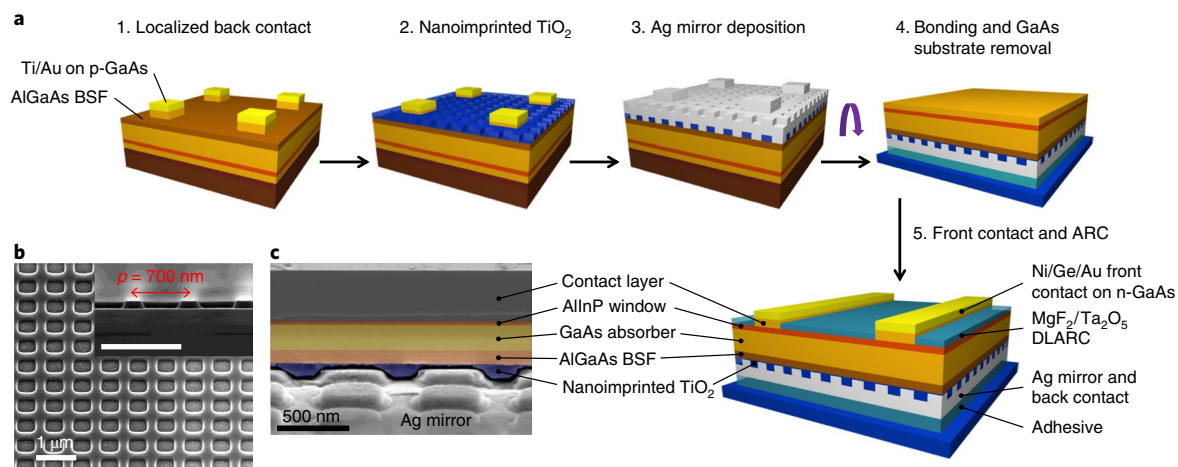


Fig. 1 | Fabrication process for ultrathin GaAs solar cells with a nanostructured back mirror. **a**, Sketches of the main fabrication steps. **b**, SEM image of nano-imprinted TiO₂ periodic structures before Ag mirror deposition. Inset: cross-section of the TiO₂. Scale bar, 1 μm. **c**, SEM cross-sectional view after removing the GaAs substrate, showing the Ag nanostructured back mirror.

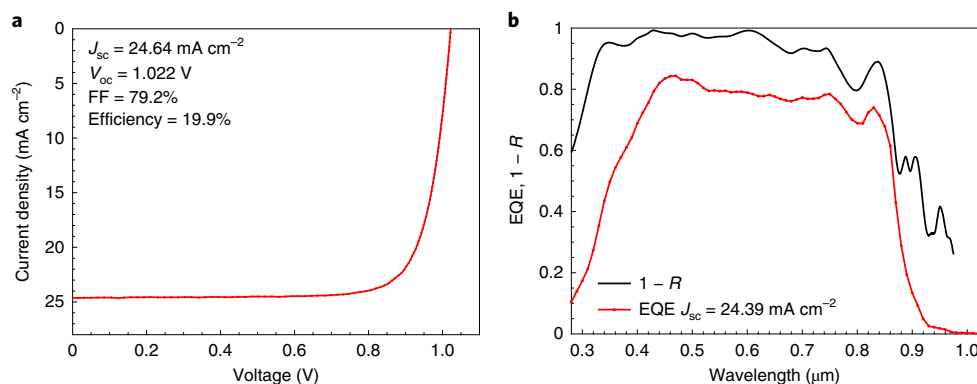


Fig. 2 | Best ultrathin solar cell based on a 205-nm-thick GaAs absorber and a nanostructured Ag mirror. **a, b**, J - V characteristics (**a**) and EQE (**b**) of the 19.9%-efficient solar cell with an aperture area of 4.02 mm² measured at the Fraunhofer ISE calibration laboratory under standard conditions (AM1.5G, 1,000 W m⁻², 25 °C). The black curve of $1 - R$ (R , specular reflectance) in **b** exhibits multi-resonant features in agreement with the EQE.

EQE exhibits less pronounced resonances due to fabrication imperfections, but a similar average absorption. The cross-sectional maps of the generation rates displayed in Fig. 3c for 1-μm-thick GaAs solar cells and structures A, B and C illustrate the spectacular increase in the density of photogenerated carriers as a result of efficient light trapping in a 205-nm-thick GaAs layer.

To gain more insight into the mechanism of the optical resonances, labelled α , β and γ in Fig. 3b, we calculate $1 - R$, where R is the specular reflectance at normal incidence as a function of the wavelength and grating period p . Figure 3e shows the result obtained for a nanostructured TiO₂/Ag back mirror with a fixed grating height of $h = 120$ nm and a square width-to-period ratio of $d/p = 0.6$. This dispersion diagram features numerous resonances with two different behaviours. In the 400–600 nm wavelength range, absorption peaks are insensitive to the grating period. These resonances are attributed to vertical Fabry–Perot (FP) modes. The same features can be observed with a flat mirror, and the resonance wavelengths depend mainly on the total thickness of the layer stack. The resonant conditions are given by

$$2 \sum_i k_{z,i} h_i + \varphi = 2\pi q \quad (1)$$

where $k_{z,i} = 2\pi n_i / \lambda$ is the z -component wavevector at normal incidence in layer i (thickness h_i and refractive index n_i), λ is the

wavelength and the integer q defines the FP order. The phase change φ induced by reflection at the top and bottom interfaces is evaluated from the complex Fresnel coefficients. The result is shown in Fig. 3e (green dashed lines) for the two FP resonances α_1 and α_2 found at short wavelengths. They correspond to FP orders $q = 6$ and $q = 7$ (labelled FP₆ and FP₇, respectively). The low contrast of these resonance peaks is due to the high absorption and efficient DLARC in this wavelength range.

In the long-wavelength range ($\lambda > 600$ nm), the absorption peaks exhibit a strong period dependence and are attributed to guided-mode resonances. The grating scatters light into diffracted waves of orders (m_1, m_2) defined by their in-plane wavevectors:

$$\mathbf{k}_{\parallel(m_1, m_2)} = \mathbf{k}_{\parallel(00)} + m_1 \frac{2\pi}{p} \mathbf{e}_x + m_2 \frac{2\pi}{p} \mathbf{e}_y \quad (2)$$

where $\mathbf{k}_{\parallel(00)}$ is the in-plane wavevector of incident waves and (m_1, m_2) are integers. The additional in-plane momentum induced by the grating allows coupling through either transverse-electric (TE) or transverse-magnetic (TM) guided waves propagating in the solar cells. The approximate resonance wavelengths are calculated using a model of the planar waveguide³⁵, taking into account the quasi-periodic boundary condition for the in-plane component (equation (2)).

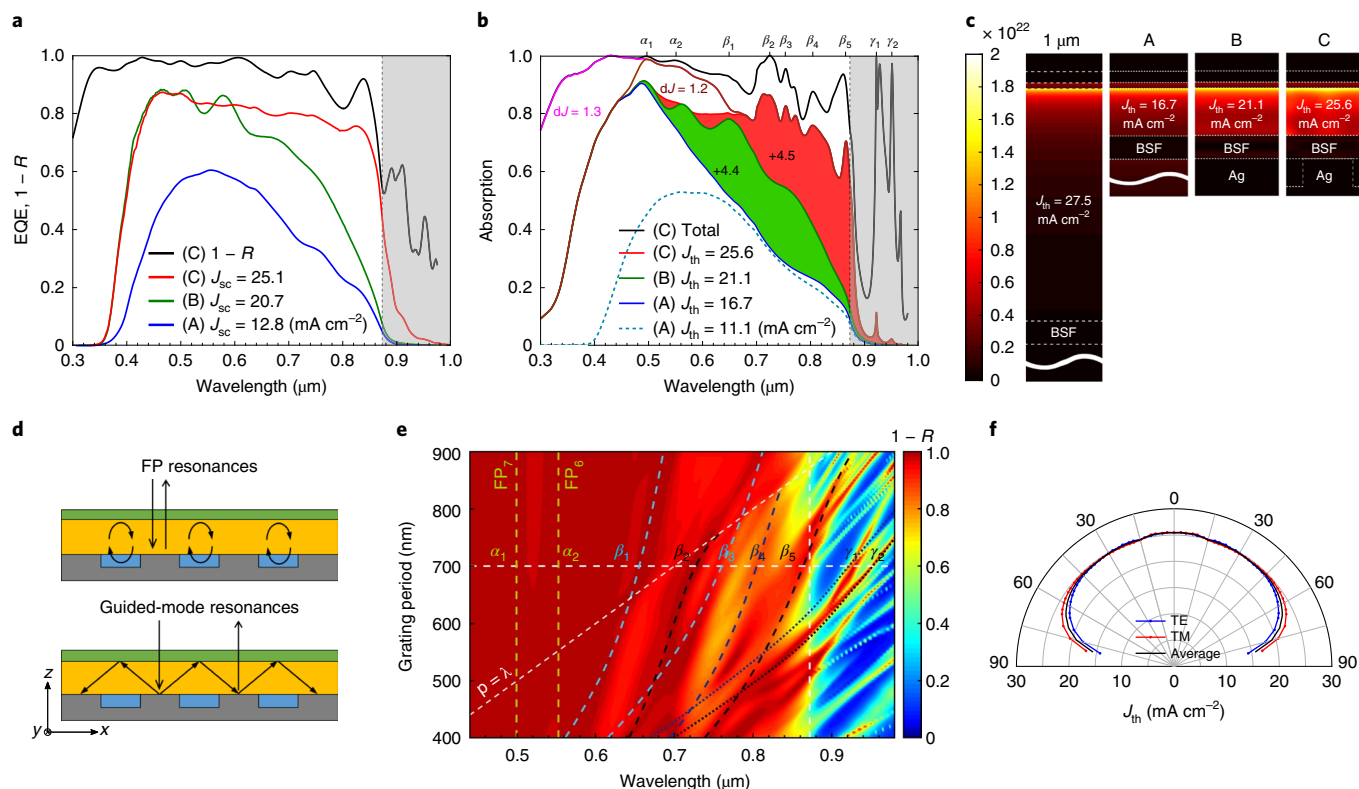


Fig. 3 | Optical analysis of the ultrathin GaAs solar cells. **a**, EQE measurements for three different types of solar cell: as-grown on a GaAs substrate (A), with a flat Ag back mirror (B) and with a nanostructured Ag back mirror (C). A plot of $1 - R$ (solar cell C) is also shown (black curve). **b**, Calculation of optical absorption in 205-nm-thick GaAs for the same structures. Structure A, as-grown with a single-layer ARC (dashed line) or with the same design as B (reverse order, without a back mirror, solid line). For structure C, detailed absorption in each III-V layer is shown (AlInP sum up to $dJ = 1.3 \text{ mA cm}^{-2}$; AlGaAs, $dJ = 1.2 \text{ mA cm}^{-2}$). The shaded area in **a** and **b** shows the spectral region of photon energies below the GaAs bandgap. **c**, Cross-sectional maps of the generation rate in 1- μm -thick GaAs solar cells (DLARC, as-grown) and structures A, B and C (Supplementary Note 2). **d**, Schematic of the different types of resonance. **e**, Dispersion diagram of $1 - R$ as a function of the illumination wavelength and the period of the diffraction grating. Dashed curves are resonance wavelengths calculated with analytical models (see main text for details). **f**, Polar plot of the calculated J_{sc} as a function of the incident angle in 205-nm-thick GaAs (structure C). TM, transverse magnetic; TE, transverse electric.

The coupling between guided modes is not taken into account in this simple model. Nevertheless, it allows us to fit and to identify the main resonances: β_1 and β_3 are TE guided modes coupled to diffracted orders $(\pm 1, \pm 1)$, β_2 and β_5 are TM guided modes coupled to diffracted orders $(\pm 1, 0)$, β_4 is the TE guided mode coupled to diffracted orders $(\pm 1, 0)$ and γ_1 and γ_2 are TE and TM guided modes coupled to diffracted orders $(\pm 2, 0)$. The corresponding dispersion curves are plotted in Fig. 3e and agree with rigorous numerical calculations. They exhibit different slopes related to the different diffracted orders. The origin and characteristics of both FP and guided-mode resonances are further confirmed by their angular dependence, and by the number and position of nodes and anti-nodes in the field distributions (Supplementary Notes 1 and 3 and Supplementary Figs. 5 and 7). Overall, the integrated absorption maintains a high short-circuit current ($J_{th} > 25 \text{ mA cm}^{-2}$ up to 45° , $J_{th} > 23.5 \text{ mA cm}^{-2}$ up to 60°) through overlaps of multiple resonances (Fig. 3f).

Loss analysis and path towards 25% efficiency

In this section, we analyse the performance of the ultrathin solar cell with a nanostructured mirror and discuss the possibility to achieve even higher efficiency. Figure 4a summarizes the detailed loss analysis for J_{sc} , FF and V_{oc} : our experimental results are shown in bold and the top values correspond to radiative limits. The J_{sc} reference of 31.9 mA cm^{-2} is calculated for 205-nm-thick GaAs using an approximate Lambertian light trapping model^{5,6}. We measured $J_{sc} = 24.6 \text{ mA cm}^{-2}$, and the highest EQE without front contact

shading (5–6% of the total area) results in $J_{sc} = 25.1 \text{ mA cm}^{-2}$, close to the numerical calculation of 25.6 mA cm^{-2} for the optimized TiO_2/Ag back mirror. The small discrepancy is due to the shape of the fabricated structures. Parasitic optical losses include absorption in the window layer ($dJ = 1.3 \text{ mA cm}^{-2}$), in the BSF ($dJ = 1.2 \text{ mA cm}^{-2}$), in the Ag mirror ($dJ = 2.7 \text{ mA cm}^{-2}$) and due to reflection ($dJ = 1.1 \text{ mA cm}^{-2}$). Parasitic absorption in the metallic reflector can be avoided through a combination of high-index-contrast gratings with all-dielectric or hybrid dielectric/metallic mirrors^{36,37}. The stack of semiconductor heterostructures requires further optimization to reduce the thickness of the AlInP and AlGaAs layers and improve the collection of photogenerated carriers in these layers. The shape of the nanostructured back mirror could also be optimized to improve light trapping. For example, replacing squares by an L-shape or using blazed nanostructures breaks a plane of symmetry and should increase the number of resonance modes by a factor of two. Overall, assuming half of the optical losses are recovered leads to a short-circuit current of over 28 mA cm^{-2} .

To analyse the electronic characteristics of the solar cells, 1 sun $J - V$ curves were fitted using a two-diode model with fixed J_{sc} and diode idealities of 1 and 2³⁸. An example fit is given in Fig. 4b, showing the absolute values of $J(V) - J_{sc}$ in a logarithmic scale and different components of the two-diode model. The fitted parameters are $J_{01} = 2.8 \times 10^{-17} \text{ mA cm}^{-2}$, $J_{02} = 4.3 \times 10^{-8} \text{ mA cm}^{-2}$, $R_p = 2.4 \times 10^3 \Omega \text{ cm}^2$ and $R_s = 0.8 \Omega \text{ cm}^2$. This procedure was repeated for every solar cell with different surface areas of 1×1 , 2×2 and

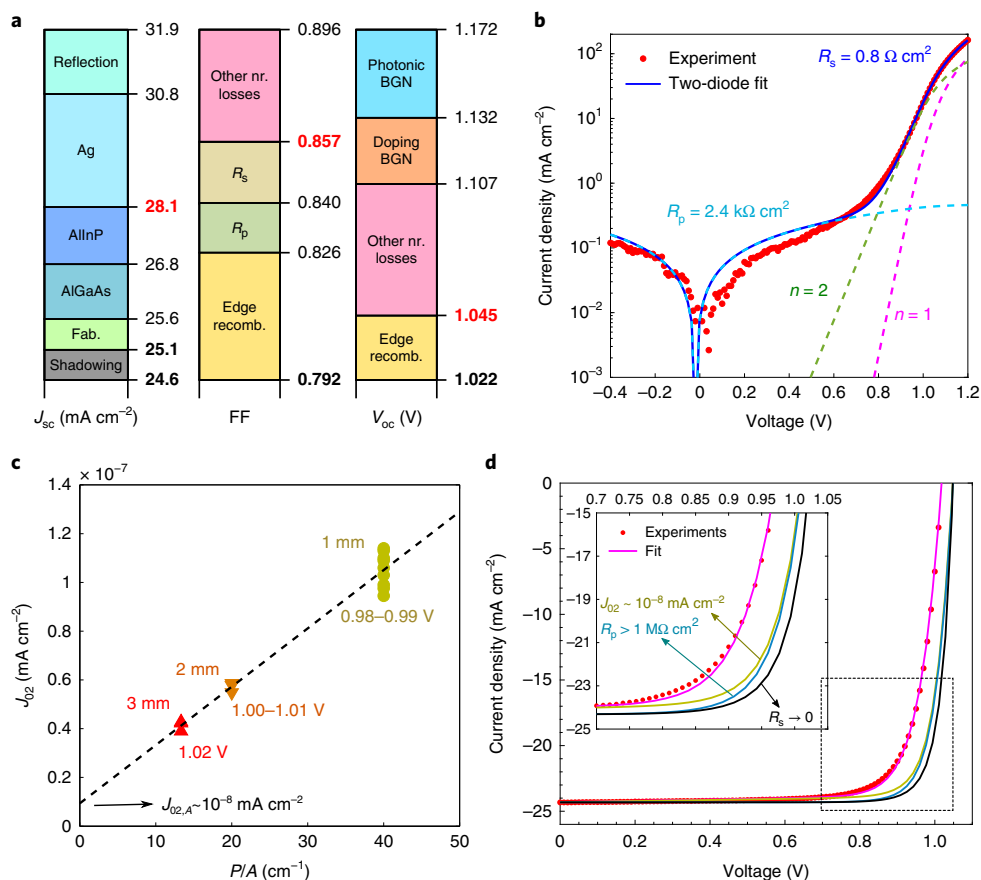


Fig. 4 | $J-V$ characteristics and loss analysis. **a**, Detailed loss analysis for J_{sc} , FF and V_{oc} . Different colours represent the different origins of losses, including non-radiative (nr.) losses, that fill the gap between the measurements (bold) and the radiative limit for a 205 nm GaAs absorber (top values). Intermediate values in red appear as a realistic short-term target that corresponds to a conversion efficiency of 25%. **b**, Typical $J-V$ curve under 1 sun illumination shifted by J_{sc} in log scale (red dots, $J - J_{sc}$) and fit with a two-diode model (blue curve). Different components of the model are shown as dashed lines (n , ideality factor of the diodes). **c**, Correlation of the J_{02} saturation current density with the perimeter-to-surface ratio P/A . Dashed line, linear fit of J_{02} values extracted from square solar cells of width 3 mm (three devices), 2 mm (three devices) and 1 mm (nine devices) (Supplementary Figs. 2 and 3). **d**, $J-V$ characteristics of the best solar cell under 1 sun illumination and the fit. Efficiency can be increased by successive improvements of the fitted parameters (see main text): saturation current density J_{02} (yellow green curve), shunt resistance (blue curve) and series resistance (black curve). Inset: enlarged view around the maximum power point.

$3 \times 3 \text{ mm}^2$. V_{oc} decreases with cell size and is correlated with an increased dark current density J_{02} . The size dependence of the recombination current is observed in GaAs³⁹ and can be recovered through edge passivation using S-based chemicals⁴⁰. In Fig. 4c, we plot the J_{02} values as a function of the perimeter-to-surface ratio (P/A). The linear trend allows us to decompose J_{02} into a surface area component $J_{02,A}$ and a perimeter component $J_{02,P}$ ⁴¹

$$J_{02} = J_{02,A} + J_{02,P} \frac{P}{A} \quad (3)$$

For large-area solar cells, edge recombination is suppressed. J_{02} reaches $J_{02,A} = 8.7 \times 10^{-9} \text{ mA cm}^{-2}$ and results in an increase of V_{oc} up to 1.045 V and FF up to 0.826. The corresponding $J-V$ characteristics are plotted in Fig. 4d. Further improvements in FF are expected with improved parallel and series resistances: FF = 0.84 for $R_p = 10^6 \Omega \text{ cm}^2$ and FF = 0.857 for $R_s = 0$. The visible shunt conductance under illumination may be due to native oxides across the p-n junction at the edge or degradation from process steps after the mesa edges are revealed by chemical etching. The series resistance can be further optimized with GeAu alloys⁴² and a smaller spacing of contact grids. To achieve even higher FF, the dark current density J_{02} should be lowered to $\sim 10^{-9} \text{ mA cm}^{-2}$ (ref. 3).

Regarding V_{oc} , we calculate the radiative limit using the detailed balance principle applied for 205-nm-thick GaAs solar cells^{26,43,44} (Supplementary Note 5). The calculated limit efficiency (25 °C, AM1.5G spectrum illumination) is $\eta = 24.6\%$ for the cell with a flat mirror ($J_{sc} = 23.4 \text{ mA cm}^{-2}$, $V_{oc} = 1.172 \text{ V}$, FF = 0.896) and $\eta = 32.3\%$ for the cell with Lambertian light trapping ($J_{sc} = 31.9 \text{ mA cm}^{-2}$, $V_{oc} = 1.132 \text{ V}$, FF = 0.893). We note that the V_{oc} radiative limit is reduced by 40 meV for Lambertian light trapping as compared to a flat mirror because of enhanced radiative emission (photonic band-gap narrowing, BGN). However, most of the V_{oc} loss in our devices originates from non-radiative recombination (Fig. 4d). The choice of high doping is favourable for lateral conductivity and a high built-in potential in an ultrathin absorber, but p-type GaAs is known for the BGN effect, which lowers the bandgap by $\sim 26 \text{ meV}$ at a doping concentration of 10^{18} cm^{-3} (ref. 45). To achieve high V_{oc} , reducing the non-radiative loss and maintaining efficient photon recycling are of utmost importance. Based on this discussion, an efficiency of 25% ($J_{sc} = 28 \text{ mA cm}^{-2}$, $V_{oc} = 1.05 \text{ V}$, FF = 0.85) appears to be a realistic target for 205-nm-thick GaAs solar cells with optimized design.

Conclusion

In summary, we have conceived and fabricated ultrathin GaAs solar cells with a TiO_2/Ag nanostructured back mirror using soft

nanoimprint lithography. We have achieved a certified efficiency of 19.9% under AM1.5G illumination ($J_{sc} = 24.64 \text{ mA cm}^{-2}$, $V_{oc} = 1.022 \text{ V}$, $FF = 0.792$). The EQE exhibits a strong absorption enhancement in the 600–900 nm wavelength range, in agreement with numerical calculations. Broadband absorption is the result of multiple overlapping resonances induced by the nanostructured mirror, identified as FP and guided-mode resonances. We have revealed the origin of optical and electrical losses and proposed routes for further optimizations so that a 200-nm-thick ultrathin GaAs solar cell with 25% efficiency appears as a realistic short-term target. These results constitute a very significant improvement over previous experimental achievements and numerical predictions of realistic devices and demonstrate that broadband light trapping is compatible with high performance. These results can find direct applications in flexible, lightweight and radiation-resistant photovoltaic system for space applications. For large-scale photovoltaics, applying a similar architecture to thin-film solar cells made of CIGS and CdTe opens up promising perspectives for material savings and throughput improvements. In this context, this approach based on nanoimprinting sol-gel could represent a game changer for low-cost and large-scale fabrication of nanostructured mirrors compatible with industrial constraints.

Methods

Semiconductor layer stack. The III–V semiconductor layers were grown by MOVPE at the Fraunhofer Institute for Solar Energy Systems (ISE). The layers' target thicknesses and doping levels are provided in Supplementary Table 1. Zn and Si were used as p-type and n-type dopants, respectively. The growth was conducted on an n-type GaAs(100) substrate, consisting of buffer GaAs, AlGaAs etch stop (used for substrate removal), n+ GaAs/GaInAs contact layers, n AlInP window, 205 nm GaAs homojunction as the main absorber, p AlGaAs BSF and p+ GaAs contact layer. Wide-bandgap AlGaAs and AlInP alloys were used to passivate the GaAs surface and act as a minority carrier blocking layer to reduce surface recombination losses. The fabrication processes were performed at the Centre for Nanoscience and Nanotechnology (C2N) and are sketched in Fig. 1.

Localized back contact fabrication. The localized p-type back contacts consisted of $5 \times 5 \mu\text{m}^2$ squares regularly spaced with a period of $50 \mu\text{m}$ in both x and y directions on the layer surface defined using photolithography (coverage, 1% of the total surface). After deoxidation of p+ GaAs in a dilute HCl solution, localized Ti/Au (20/200 nm) was fabricated using electron-beam assisted evaporation and liftoff. The uncovered area of p+ GaAs was etched in a mixture of citric acid at 1 g l^{-1} and hydrogen peroxide (30%) with a 5:1 volume ratio. Etching was naturally stopped at the top of the AlGaAs layer (BSF).

Nanostructured TiO_2/Ag mirror fabrication. After localized back contacts fabrication, a dielectric mirror was fabricated by directly embossing a TiO_2 sol-gel derived film followed by Ag deposition. To emboss the film, we used degassing assisted patterning (DAP)⁴⁶, a modified version of soft nanoimprint lithography that allows rapid embossing of sol-gel derived films⁴⁷. The technique makes use of a degassed polydimethylsiloxane (PDMS)-based stamp to improve the resolution and rapidity of the embossing of the films. Unlike other nanoimprint techniques, replication by DAP is driven by the inner underpressure of the stamp, and therefore does not require the use of an embossing machine. Because no external pressure is applied, DAP induces no long-range pattern deformations, limits short-range deformations and is thus suitable for large-surface-area patterning. The PDMS-based stamp was first degassed in a desiccator for 10 min. TiO_2 sol-gel hybrid was spin-coated on the AlGaAs surface (BSF) and the PDMS-based stamp was then moulded (in air). Eventual macroscopic air bubbles surrounding defects and/or localized around the localized back contacts were removed within a few seconds by diffusion of air in the degassed stamp. In the same way, air trapped in the stamp protrusion was taken inside the stamp and replaced by the TiO_2 sol-gel. The degassed stamp also quickly removed the ethanol and water expelled during the sol-gel transition (gelation), hydrolysis and condensation occurring when the sol-gel was stabilized at 110°C for 5 min on a hot-plate before demoulding of the stamp. Subsequently, the top surface of the sample (coated with TiO_2 nanostructures) was protected with a photoresist mask, revealing only the area of the localized ohmic contacts. The residual nanoimprinted TiO_2 above the localized contacts was etched by quickly dipping the sample in a dilute HF solution. Ag (200 nm) was then deposited by electron-beam-assisted evaporation using a rotating stage with a 10° tilt to the surface normal to ensure conformal deposition of Ag on both localized ohmic contacts and TiO_2 nanostructures. A TiO_2/Ag nanostructured back mirror was thus obtained that simultaneously acted as the back electrode.

Bonding and substrate removal. The Ag mirror side of the sample was bonded to a glass host substrate using OrmoStamp (micro resist technology GmbH, a

flexible hybrid inorganic/organic polymer), which was reticulated under ultraviolet light for 20 min. The GaAs substrate was etched in a $\text{NH}_4\text{OH}:\text{H}_2\text{O}_2:\text{H}_2\text{O}$ (1:4:15) solution and the AlGaAs etch stop was removed in $\text{HF}:\text{H}_2\text{O}$ (1:20). After this step, the III–V layer stack order was inverted.

Front contacts and ARC. The front contacts, with a grid spacing of 600 or $800 \mu\text{m}$, were fabricated using steps similar to those used for the localized back contacts. The contacts consist of multilayers of Ni/Au/Ge/Au/Ni/Au (4/10/60/110/10/100 nm) with no post thermal annealing to avoid degradation of the Ag mirror as well as the ultrathin GaAs absorber. Uncovered areas of n GaAs and n $\text{Ga}_{0.87}\text{In}_{0.13}\text{As}$ were etched in a mixture of citric acid at 1 g l^{-1} and hydrogen peroxide (30%) with a 5:1 volume ratio. The final solar cells with areas of 1×1 , 2×2 and $3 \times 3 \text{ mm}^2$ were delimited with a photolithography mask and mesa etching in dilute HCl (removing AlInP) and $\text{H}_3\text{PO}_4:\text{H}_2\text{O}_2:\text{H}_2\text{O}$ (3:1:40) (removing GaAs). The $\text{MgF}_2/\text{Ta}_2\text{O}_5$ (78/48 nm) DLARC was deposited using electron-beam-assisted evaporation.

Description of the silicon master, PDMS-based stamp and sol-gel derived film. *Silicon master fabrication.* The silicon master mould was fabricated by electron-beam lithography carried out at 100 keV (Vistec EBPG5000+) using positive-tone PMMA resist (495PMMA A – solids: 7% in anisole) and anisotropic reactive ion etching based on SF_6/CHF_3 gases. The silicon master was treated with 1H,1H,2H,2H-perfluorooctyltriethoxysilane (POTS) using a chemical vapour deposition (CVD) method, following a procedure developed in ref. 48.

Hard-PDMS/PDMS stamp fabrication. The silicon master was replicated into a composite hard-PDMS/PDMS stamp using a procedure similar to the one proposed in ref. 49. The hard-PDMS/PDMS stamp was finally treated with trimethylsilyl chloride silanes using a CVD method⁵⁰.

Sol-gel initial solutions. Absolute ethanol was purchased from Normapur and inorganic precursor TiCl_4 and F127 Pluronic ($\text{EO}_{106}\text{-PO}_{70}\text{-EO}_{106}$) were purchased from Aldrich. Dense TiO_2 thin films were prepared by spin-coating solutions composed of $\text{TiCl}_4:\text{F127}:\text{H}_2\text{O}:\text{EtOH}$ in a molar ratio of 1:0.0001:10:50. The final solution was obtained by dissolving the precursor TiCl_4 in ethanol and water followed by addition of a small amount of F127 (to improve wettability).

Optical simulations and refractive indices. Optical simulations were performed using the RCWA method^{51–54}. We chose the x – z plane as the plane of incidence and considered the impinging plane waves to be linearly polarized. We call TE the incident polarization for the electric field perpendicular to the incidence plane (along the y axis), and TM the incident polarization for the magnetic field perpendicular to the incidence plane. We calculated the absorption in each layer with 20 Fourier orders, and the calculation was performed for each wavelength. The refractive indices used for optical simulation of ultrathin GaAs solar cells are plotted in Supplementary Fig. 4. The refractive indices are taken from ref. 51 for Ta_2O_5 , from ref. 52 for MgF_2 and $\text{Al}_{0.42}\text{Ga}_{0.58}\text{As}$ and from ref. 53 for $\text{Al}_{0.51}\text{In}_{0.49}\text{P}$. We used the refractive indices of high-purity GaAs^{52,54}, and we fitted the near bandgap extinction coefficients with a cubic spline and extended the data in the sub-bandgap region with an exponential Urbach tail of energy width 10 meV for n GaAs and 20 meV for p GaAs. A larger band tail is attributed for p GaAs to simulate the higher sub-bandgap absorption. The refractive index of Ag was taken from the measurements published recently in ref. 55 to account for realistic absorption losses in Ag. TiO_2 , prepared from sol-gel using our process has a typical refractive index of ~ 1.9 at 500 nm, and kept constant over the whole spectrum.

Optimization of the optical design. The geometry of the ultrathin GaAs solar cells was optimized by maximizing the theoretical short-circuit current J_{th} . For the DLARC on ultrathin GaAs solar cells with a flat mirror, the best value was obtained for $\text{MgF}_2/\text{Ta}_2\text{O}_5$ layers of thickness 78/48 nm. For ultrathin GaAs solar cells with a nanostructured Ag back mirror, we used the same DLARC and determined the optimal geometry as a grating height of $h = 120 \text{ nm}$, period $p = 700 \text{ nm}$ and silver square nanostructures of width 420 nm (60% of the period).

Reporting Summary. Further information on research design is available in the Nature Research Reporting Summary linked to this article.

Data availability

The data that support the plots within this paper and other findings of this study are available from the corresponding author upon reasonable request.

Received: 27 December 2018; Accepted: 10 June 2019;

Published online: 05 August 2019

References

1. Yoshikawa, K. et al. Silicon heterojunction solar cell with interdigitated back contacts for a photoconversion efficiency over 26%. *Nat. Energy* 2, 17032 (2017).

2. Shockley, W. & Queisser, H. J. Detailed balance limit of efficiency of p–n junction solar cells. *J. Appl. Phys.* **32**, 510–519 (1961).
3. Kayes, B. M. et al. 27.6% conversion efficiency, a new record for single-junction solar cells under 1 sun illumination. In *Proc. 2011 37th IEEE Photovoltaic Specialists Conference (PVSC)* 000004–000008 (IEEE, 2011).
4. Green, M. A. et al. Solar cell efficiency tables (Version 53). *Prog. Photovolt.* **27**, 3–12 (2019).
5. Green, M. A. Lambertian light trapping in textured solar cells and light-emitting diodes: analytical solutions. *Prog. Photovolt.* **10**, 235–241 (2002).
6. Yablonoitch, E. Statistical ray optics. *J. Opt. Soc. Am.* **72**, 899–907 (1982).
7. Hirst, L. C. et al. Intrinsic radiation tolerance of ultra-thin GaAs solar cells. *Appl. Phys. Lett.* **109**, 033908 (2016).
8. Brongersma, M. L., Cui, Y. & Fan, S. Light management for photovoltaics using high-index nanostructures. *Nat. Mater.* **13**, 451–460 (2014).
9. Collin, S. Nanostructure arrays in free-space: optical properties and applications. *Rep. Prog. Phys.* **77**, 126402 (2014).
10. Mokkaapati, S. & Catchpole, K. R. Nanophotonic light trapping in solar cells. *J. Appl. Phys.* **112**, 101101 (2012).
11. Depauw, V. et al. Sunlight-thin nanophotonic monocrystalline silicon solar cells. *Nano Futures* **1**, 021001 (2017).
12. Branham, M. S. et al. 15.7% efficient 10- μm -thick crystalline silicon solar cells using periodic nanostructures. *Adv. Mater.* **27**, 2182–2188 (2015).
13. Gaucher, A. et al. Ultrathin epitaxial silicon solar cells with inverted nanopyramid arrays for efficient light trapping. *Nano Lett.* **16**, 5358–5364 (2016).
14. Wang, K. X., Yu, Z., Liu, V., Cui, Y. & Fan, S. Absorption enhancement in ultrathin crystalline silicon solar cells with antireflection and light-trapping nanocone gratings. *Nano Lett.* **12**, 1616–1619 (2012).
15. Kapur, P. et al. A manufacturable, non-plated, non-Ag metallization based 20.44% efficient, 243 cm^2 area, back contacted solar cell on 40 μm thick mono-crystalline silicon. In *Proc. 28th European Photovoltaic Solar Energy Conference and Exhibition 2228–2231* (WIP Renewable Energies, 2013).
16. Cariou, R. et al. III–V-on-silicon solar cells reaching 33% photoconversion efficiency in two-terminal configuration. *Nat. Energy* **3**, 326–333 (2018).
17. Goffard, J. et al. Light trapping in ultrathin CIGS solar cells with nanostructured back mirrors. *IEEE J. Photovolt.* **7**, 1433–1441 (2017).
18. van Lare, C., Yin, G., Polman, A. & Schmid, M. Light coupling and trapping in ultrathin Cu(In,Ga)Se₂ solar cells using dielectric scattering patterns. *ACS Nano* **9**, 9603–9613 (2015).
19. Söderström, K., Haug, F.-J., Escarré, J., Cubero, O. & Ballif, C. Photocurrent increase in n–i–p thin film silicon solar cells by guided mode excitation via grating coupler. *Appl. Phys. Lett.* **96**, 213508 (2010).
20. Zhu, J., Hsu, C.-M., Yu, Z., Fan, S. & Cui, Y. Nanodome solar cells with efficient light management and self-cleaning. *Nano Lett.* **10**, 1979–1984 (2010).
21. Liu, W. et al. Surface plasmon enhanced GaAs thin film solar cells. *Sol. Energy Mater. Sol. Cells* **95**, 693–698 (2011).
22. Nakayama, K., Tanabe, K. & Atwater, H. A. Plasmonic nanoparticle enhanced light absorption in GaAs solar cells. *Appl. Phys. Lett.* **93**, 121904 (2008).
23. Massiot, I. et al. Metal nanogrid for broadband multiresonant light-harvesting in ultrathin GaAs layers. *ACS Photon.* **1**, 878–884 (2014).
24. Atwater, H. A. & Polman, A. Plasmonics for improved photovoltaic devices. *Nat. Mater.* **9**, 205–213 (2010).
25. Vandamme, N. et al. Ultrathin GaAs solar cells with a silver back mirror. *IEEE J. Photovolt.* **5**, 565–570 (2015).
26. Miller, O. D., Yablonoitch, E. & Kurtz, S. R. Strong internal and external luminescence as solar cells approach the Shockley–Queisser limit. *IEEE J. Photovolt.* **2**, 303–311 (2012).
27. Steiner, M. A. et al. Optical enhancement of the open-circuit voltage in high quality GaAs solar cells. *J. Appl. Phys.* **113**, 123109 (2013).
28. Walker, A. W. et al. Impact of photon recycling on GaAs solar cell designs. *IEEE J. Photovolt.* **5**, 1636–1645 (2015).
29. Yang, W. et al. Ultra-thin GaAs single-junction solar cells integrated with a reflective back scattering layer. *J. Appl. Phys.* **115**, 203105 (2014).
30. Lee, S.-M. et al. High performance ultrathin GaAs solar cells enabled with heterogeneously integrated dielectric periodic nanostructures. *ACS Nano* **9**, 10356–10365 (2015).
31. Hugonin, J. P. & Lalanne, P. Reticolo (IOTA/CNRS, 2005); <https://www.lp2n.institutoptique.fr/Membres-Services/Responsables-d-equipe/LALANNE-Philippe>
32. Lalanne, P. & Jurek, M. P. Computation of the near-field pattern with the coupled-wave method for transverse magnetic polarization. *J. Mod. Opt.* **45**, 1357–1374 (1998).
33. Lalanne, P. & Morris, G. M. Highly improved convergence of the coupled-wave method for TM polarization. *J. Opt. Soc. Am. A* **13**, 779–784 (1996).
34. Li, L. New formulation of the Fourier modal method for crossed surface-relief gratings. *J. Opt. Soc. Am. A* **14**, 2758–2767 (1997).
35. Yeh, P. *Optical Waves in Layered Media* (Wiley, 1988).
36. Barugkin, C., Beck, F. J. & Catchpole, K. R. Diffuse reflectors for improving light management in solar cells: a review and outlook. *J. Opt.* **19**, 014001 (2017).
37. Fu, S. M. et al. Approaching conversion limit with all-dielectric solar cell reflectors. *Opt. Express* **23**, A106–A117 (2015).
38. Suckow, S. 2–3 diode fit. *NanoHub* (2014); <https://nanohub.org/resources/14300>
39. Ochoa, M., Algora, C., Espinet-González, P. & García, I. 3-D modeling of perimeter recombination in GaAs diodes and its influence on concentrator solar cells. *Sol. Energy Mater. Sol. Cells* **120**, 48–58 (2014).
40. Sheldon, M. T., Eisler, C. N. & Atwater, H. A. GaAs passivation with trioctylphosphine sulfide for enhanced solar cell efficiency and durability. *Adv. Energy Mater.* **2**, 339–344 (2012).
41. Espinet-González, P. et al. Analysis of perimeter recombination in the subcells of GaInP/GaAs/Ge triple-junction solar cells. *Prog. Photovolt. Res. Appl.* **23**, 874–882 (2015).
42. Shen, T. C., Gao, G. B. & Morko, H. Recent developments in ohmic contacts for III–V compound semiconductors. *J. Vac. Sci. Technol. B* **10**, 2113 (1992).
43. Sandhu, S., Yu, Z. & Fan, S. Detailed balance analysis of nanophotonic solar cells. *Opt. Express* **21**, 1209–1217 (2013).
44. Xu, Y., Gong, T. & Munday, J. N. The generalized Shockley–Queisser limit for nanostructured solar cells. *Sci. Rep.* **5**, 13536 (2015).
45. Jain, S. C., McGregor, J. M. & Roulston, D. J. Band-gap narrowing in novel III–V semiconductors. *J. Appl. Phys.* **68**, 3747–3749 (1990).
46. Luo, C., Ni, X., Liu, L., Nomura, S. M. & Chen, Y. Degassing-assisted patterning of cell culture surfaces. *Biotechnol. Bioeng.* **105**, 854–859 (2010).
47. Dalstein, O. et al. Nanoimprinted, submicrometric, MOF-based 2D photonic structures: toward easy selective vapors sensing by a smartphone camera. *Adv. Funct. Mater.* **26**, 81–90 (2016).
48. Wang, L., Wei, J. & Su, Z. Fabrication of surfaces with extremely high contact angle hysteresis from polyelectrolyte multilayer. *Langmuir* **27**, 15299–15304 (2011).
49. Odom, T. W., Love, J. C., Wolfe, D. B., Paul, K. E. & Whitesides, G. M. Improved pattern transfer in soft lithography using composite stamps. *Langmuir* **18**, 5314–5320 (2002).
50. Cattoni, A., Cambri, E., Decanini, D., Faini, G. & Haghiri-Gosnet, A. M. Soft UV-NIL at 20 nm scale using flexible bi-layer stamp casted on HSQ master mold. *Microelectron. Eng.* **87**, 1015–1018 (2010).
51. Gao, L., Lemarchand, F. & Lequime, M. Exploitation of multiple incidences spectrometric measurements for thin film reverse engineering. *Opt. Express* **20**, 15734–15751 (2012).
52. Palik, E. D. *Handbook of Optical Constants of Solids* (Academic Press, 1997).
53. Schubert M. & Woollam J. A. Isotropic dielectric functions of highly disordered Al_xGa_{1-x}InP (0 ≤ x ≤ 1) lattice matched to GaAs. *J. Appl. Phys.* **86**, 2025 (1999).
54. Sturge, M. D. Optical absorption of gallium arsenide between 0.6 and 2.75 eV. *Phys. Rev.* **127**, 768–773 (1962).
55. Jiang, Y., Pillai, S. & Green, M. A. Realistic silver optical constants for plasmonics. *Sci. Rep.* **6**, 30605 (2016).

Acknowledgements

The authors acknowledge discussions with J.-F. Guillemoles, electromagnetic simulation support from P. Lalanne, J.-P. Hugonin and C. Sauvan and financial support through French ANR project NANOCELL (grant no. ANR-15-CE05-0026) and the French Renatech network.

Author contributions

H.-L.C. carried out most of the fabrication steps for the solar cell experiments at C2N and performed optical modelling and results analysis. A.W.W., O.H., D.L. and F.D. designed the optimized GaAs solar cell layer structure, D.L. wrote the recipe for epitaxy growth and G.S. evaluated the characterization results in the Fraunhofer ISE CalLab. H.-L.C., A.C., R.D.L., M.F., N.V., J.G., B.B., C.D. and N.B. developed and optimized the fabrication process. A.C. and M.F. specifically developed the nanoimprint process for TiO₂ sol–gel films. N.V. contributed to the design and modelling of the devices. A.C. and S.C. developed the concept of ultrathin solar cells with a nanostructured back mirror and supervised the project. H.-L.C. and S.C. wrote the manuscript. All authors participated in the discussions and improvements of the manuscript.

Competing interests

The authors declare no competing interests.

Additional information

Supplementary information is available for this paper at <https://doi.org/10.1038/s41560-019-0434-y>.

Reprints and permissions information is available at www.nature.com/reprints.

Correspondence and requests for materials should be addressed to S.C.

Publisher's note: Springer Nature remains neutral with regard to jurisdictional claims in published maps and institutional affiliations.

© The Author(s), under exclusive licence to Springer Nature Limited 2019